Available online at www.sciencedirect.com
ScienceDirect
Computers and Mathematics with Applications 55 (2008) 1492–1502
An International Journal
computers & mathematics
with applications
www.elsevier.com/locate/camwa

A lattice Boltzmann model for contact-line motions

A. Kawasaki, J. Onishi, Y. Chen*, H. Ohashi

Department of Quantum Engineering and Systems Science, University of Tokyo, 7-3-1 Hongo, Bunkyo-ku, Tokyo 113-8656, Japan

Abstract

We develop a mesoscopic model for fluid–fluid–solid contact-line motions in the framework of the multi-component lattice Boltzmann model proposed by Gunstensen et al. [A.K. Gunstensen, D.H. Rothman, S. Zaleski, G. Zanetti, Lattice Boltzmann model of immiscible fluid, Phys. Rev. A 43 (1991) 4320–4327]. Regarding a solid wall as a motionless and undeformable fluid, this model can treat both fluid–fluid and fluid–solid interfaces in a unified way. In this research, we investigate fundamental characteristics of our model, such as the dependency of the slip velocity against the contact angles, and the dynamic contact angles against the static contact angles, and compare the simulation results with experimental observation in a qualitative sense.

Keywords: Lattice Boltzmann method; Contact-line; Contact angle; Wetting; Hysteresis

1. Introduction

The contact line, where a fluid–fluid interface intersects with a solid wall, plays an important role in hydrodynamics both in our daily life and in industrial processes, such as oil recovery from reservoirs and multi-phase flows in micro-channels. Simulation methods to deal with contact-line motions have been developed based on macroscopic hydrodynamic equations. However, there is an inconsistency in the analysis of the dynamic contact line. With the usual non-slip boundary condition, the fluid velocity on the wall is assumed to be equal to the velocity of the wall. If this condition was applied, the contact line should not move [2], which is quite different from the actual behavior of the contact line. To solve this problem, empirical slip models are introduced to the macroscopic simulation methods including the level-set method [3] and the boundary integral method [4]. Nevertheless, these slip models lack universality, in particular, in the dependency of the contact angle on the slip velocity.

Recently, the lattice Boltzmann method has also been applied to study the contact-line motions. As a model based on mesoscopic particles' motion, it does not need the prescription of the slip velocity on the solid wall. Instead, some authors [5,6] suggested a boundary condition for order parameters by specifying a contact angle for the fluid–fluid–solid contact line. In this study, we develop a novel lattice Boltzmann model for contact line through a different way of thinking. We model the contact-line motion by including terms of interfacial interaction in both the fluid and the solid phases. In our model, the contact angle is no longer a given parameter, but a quantity that

* Corresponding author.
E-mail address: chen@crimson.q.t.u-tokyo.ac.jp (Y. Chen).

0898-1221/$ - see front matter © 2008 Published by Elsevier Ltd
doi:10.1016/j.camwa.2007.08.026

emerges from the balance of interfacial tensions between the component fluids and the solid wall. In the sequel, after explanation and fundamental evaluation of our model, we will show the simulation results of the dynamic behavior of contact lines of a droplet attached on the wall in shear flow.

2. Simulation model

The lattice Boltzmann method (LBM) [7] is a fluid model with which the macroscopic flow is described by fictitious particles moving on a regular lattice. The kinetic equation for the fictitious particles is called lattice Boltzmann equation, which states the time evolution of the velocity distribution of the particles and consists of two processes: particle translation and particle collision. These processes are modeled in conformity with the molecular dynamics of real fluids. The application of LBM to the multi-component flow analysis is advocated due to its kinetic description, and a variety of multi-component models have been already proposed [1,8,9]. In order to shut off the influence from the finite width of interface and the finite miscibility of different components, the model proposed by Gunstensen et al. [1] is employed as a basis to study the contact-line motion. With this model, both the sharp interface and the complete immiscibility can be achieved.

2.1. LB multi-component model

In the multi-component model proposed by Gunstensen [1], states of each component fluid are described by the velocity distribution function of the underlying particles $f_i^\sigma(\boldsymbol{x}, t)$, which indicates the number of particles belonging to a component σ at a site $\boldsymbol{x}$ at time t with a velocity $\boldsymbol{e}_i$. The hydrodynamic variables of the fluids, mass density ρ^σ and flow velocity $\boldsymbol{u}^\sigma$ are calculated as the zeroth and the first moments of the velocity distribution functions,

$$\rho^\sigma(\boldsymbol{x}, t) = \sum_i f_i^\sigma(\boldsymbol{x}, t), \qquad \rho^\sigma(\boldsymbol{x}, t)\boldsymbol{u}^\sigma(\boldsymbol{x}, t) = \sum_i \boldsymbol{e}_i f_i^\sigma(\boldsymbol{x}, t). \tag{1}$$

The temporal evolution of the particles obeys the lattice Boltzmann equation. In the collision process, the velocity distribution of the particles relaxes to the equilibrium distribution function,

$$f_i^*(\boldsymbol{x}, t) = f_i(\boldsymbol{x}, t) - \frac{1}{\tau + 1/2}[f_i(\boldsymbol{x}, t) - f_i^{eq}(\boldsymbol{x}, t)], \tag{2}$$

where

$$f_i(\boldsymbol{x}, t) = \sum_\sigma f_i^\sigma(\boldsymbol{x}, t), \tag{3}$$

is the overall number density of particles which possess the velocity $\boldsymbol{e}_i$ in the mixture and f_i^* is the post-collision value of f_i. The equilibrium distribution f_i^{eq} is a discrete version of Maxwell–Boltzmann distribution which can be derived by the low-Mach number expansion [7],

$$f_i^{eq} = \omega_i \rho \left[1 + 3\boldsymbol{e}_i \cdot \boldsymbol{u} + \frac{9}{2}(\boldsymbol{e}_i \cdot \boldsymbol{u})^2 - \frac{3}{2}u^2\right] - \Delta f_i, \tag{4}$$

where the total mass density ρ and average fluid velocity $\boldsymbol{u}$ are calculated as,

$$\rho = \sum_\sigma \rho^\sigma, \qquad \rho\boldsymbol{u} = \sum_\sigma \rho^\sigma \boldsymbol{u}^\sigma. \tag{5}$$

The second term on the right-hand side of Eq. (4) is introduced to take account of the interface tensions between different fluid components. Unlike the original Gunstensen's model or its modified version proposed by Dupin [10], we use the following formulation for the interface tension term.

$$\Delta f_i = \frac{9}{2}\omega_i \left[\boldsymbol{e}_i \otimes \boldsymbol{e}_i - \frac{1}{3}\boldsymbol{I}\right] : \boldsymbol{T}, \tag{6}$$

where $\boldsymbol{T}$ is the total stress due to the interfacial tensions between all the possible pairs of the components,

$$\boldsymbol{T} = \sum_{(\sigma,\bar{\sigma})} \boldsymbol{T}^{\sigma\bar{\sigma}}. \tag{7}$$

The detailed form of $\boldsymbol{T}^{\sigma\bar{\sigma}}$ will be given later. By calculating the zeroth to second velocity moments of Δf_i, it is confirmed that mass and momentum conservation are satisfied and that the total stress has no unphysical dependence on fluid velocity.

$$\sum_i f_i^{eq} = \rho, \qquad \sum_i f_i^{eq} \boldsymbol{e}_i = \rho \boldsymbol{v}, \tag{8}$$

$$\sum_i f_i^{eq} \boldsymbol{e}_i \otimes \boldsymbol{e}_i = \rho \boldsymbol{v} \otimes \boldsymbol{v} + p\boldsymbol{I} - \boldsymbol{T}. \tag{9}$$

All the particles, regardless of their species, are involved in the collision process described above. The viscosity of the fluid mixture is given as $\mu = \rho\tau/3$ because a 2nd order relaxation process (Eq. (2)) is employed in the model. Note that Gunstensen-like models may become problematic when different fluid species have different densities and viscosities. In this research, all the components are assumed to have the same mass density and the same viscosity.

Another issue for the collision process is related to the miscibility among components. After the collision process, the velocity distribution for the mixture is known, but not for each fluid component. We follow a standard re-coloring technique [1] to separate the immiscible fluids. For this purpose, the so-called color potential is introduced,

$$U^{\sigma\bar{\sigma}}(\boldsymbol{x}) = -\boldsymbol{F}^{\sigma\bar{\sigma}}(\boldsymbol{x}) \cdot \boldsymbol{G}^{\sigma\bar{\sigma}}(\boldsymbol{x}), \tag{10}$$

where

$$\boldsymbol{F}^{\sigma\bar{\sigma}}(\boldsymbol{x}) = \sum_i \left\{ f_i^{\sigma,*}(\boldsymbol{x}) - f_i^{\bar{\sigma},*}(\boldsymbol{x}) \right\} \boldsymbol{e}_i, \tag{11}$$

is the color flux and

$$\boldsymbol{G}^{\sigma\bar{\sigma}}(\boldsymbol{x}) = \sum_i \omega_i \left\{ \rho^{\sigma}(\boldsymbol{x} + \boldsymbol{e}_i) - \rho^{\bar{\sigma}}(\boldsymbol{x} + \boldsymbol{e}_i) \right\} \boldsymbol{e}_i, \tag{12}$$

is the color gradient between the species σ and $\bar{\sigma}$. The post-collision velocity distribution for each component $f_i^{\sigma,*}$ is calculated such that the color potential is minimized. When this condition is achieved, the color flux is directed to the same direction of the color gradient, and thus particles of the same color are *attracted* to one another.

In the advection or the translation process, each particle migrates from its original site to one of the neighboring sites which can be determined with the discrete vectors of particle velocities,

$$f_i^{\sigma}(\boldsymbol{x} + \boldsymbol{e}_i, t + 1) = f_i^{\sigma,*}(\boldsymbol{x}, t). \tag{13}$$

This equation applies to all the components considered.

The interfacial interaction between components σ and $\bar{\sigma}$ can be calculated with the color gradient as follows,

$$\boldsymbol{T}^{\sigma\bar{\sigma}} = \kappa^{\sigma\bar{\sigma}} \boldsymbol{G}^{\sigma\bar{\sigma}} \otimes \boldsymbol{G}^{\sigma\bar{\sigma}}, \tag{14}$$

where $\kappa^{\sigma\bar{\sigma}}$ controls the strength of the interaction between the components σ and $\bar{\sigma}$. Note that the combination of Eqs. (6) and (14) leads to,

$$\Delta f_i = \frac{9}{2} \omega_i \kappa^{\sigma\bar{\sigma}} |\boldsymbol{G}^{\sigma\bar{\sigma}}|^2 \left[(\boldsymbol{e}_i \cdot \boldsymbol{n})^2 - \frac{1}{3} \right], \tag{15}$$

where $\boldsymbol{n} = \boldsymbol{G}^{\sigma\bar{\sigma}}/|\boldsymbol{G}^{\sigma\bar{\sigma}}|$ is the unit vector normal to the interface. This term will bring a perturbation to the particle distributions such that it increases the number of particles whose velocity is perpendicular to the interface while keeping the mass and the momentum conservation laws. Using such a term to describe interfacial tension was firstly introduced by Gunstensen et al. [1] for the D2Q7 model. The current model is an extension so as to be applicable to

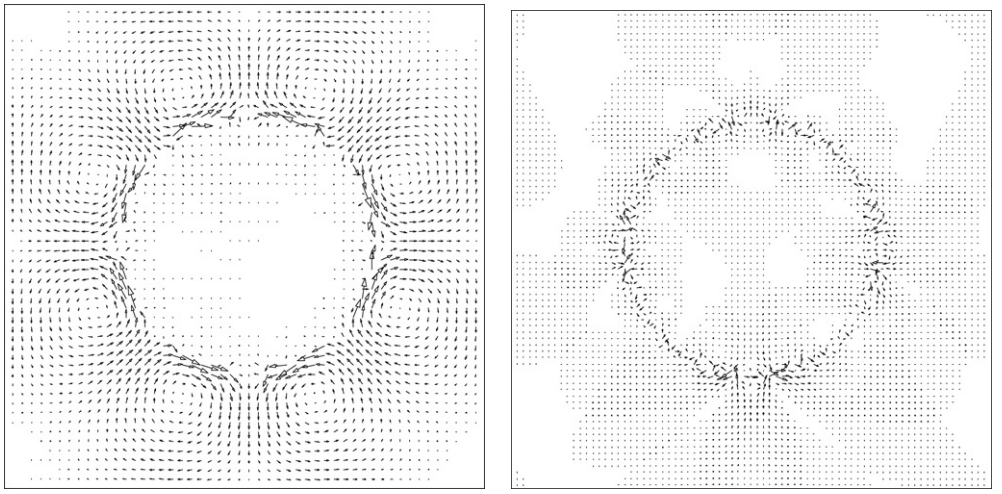

(a) Dupin model. (b) Present model.

Fig. 1. Velocity fields obtained by simulations with (a) Dupin's model and (b) our model. The drops have approximately the same radius and pressure differences inside and outside the drops have the same value with a careful tune of the interfacial tensions.

the D2Q9 model. A similar term can be found in the relatively new model proposed by Kehrwald [11], though we have neglected the normalization of the color gradient $\boldsymbol{G}^{\sigma\bar{\sigma}}$ simply due to the ease of implementation. Thus, in our model, the control parameter $\kappa^{\sigma\bar{\sigma}}$ is not the interfacial tension itself. We will discuss this issue in the next section.

2.2. Fluid–solid interface model

At the interface between fluid phase and solid phase, the bounce-back boundary condition is applied for all the components. So the fluids satisfy the non-slip conditions at the wall.

Additionally, we introduce the color interaction so as to include the fluid–solid interface tension. For this purpose, the solid wall is treated as a *stationary fluid* having a constant mass density at the boundary nodes. Thus, the relevant color gradients can be calculated in a similar way to that of fluid components.

The wetting property of solid can be controlled with the interaction parameters. For example, when the fluid phases A and B co-exist at the solid wall W, the fluid–fluid interface tension is controlled by κ^{AB}, and the fluid–solid interface tensions by κ^{AW} and κ^{BW}. However, the detailed functional form of the interface tension between the solid and the fluid phases has not been derived yet.

3. Simulation results and discussions

3.1. Validation of the interface tension model

When an immiscible droplet exists in another fluid, pressure difference between the inside and the outside of the droplet can balance the interface tension. From the viewpoint of numerical simulation, however, it is not so easy to realize the balance because of the divergence-type discretization of the surface tension term [11–13]. An unphysical mass flux, sometimes called the spurious velocity, is generated due to the error in this discretization.

Using the Gunstensen model, the interface can be made very sharp, in the mean time the spurious velocity can become very large. It motivates us to investigate the spurious velocity in the present model, and compare with that in the Dupin model [10]. Note that Gunstensen et al. originally used hexagonal lattices, and Dupin et al. modified the Gunstensen model to use the square lattice.

We simulated the stationary droplet of a radius $R = 40$ in a 150×150 square box with periodic boundary conditions. The droplet fluid has the same viscosity as that of the continuous phase, $\mu_D = \mu_C = 1/6$. We used these parameter values in both Dupin model and the present model. In Fig. 1, velocity vectors are shown. It can be found that the spurious velocity of our model is well-suppressed comparing with the Dupin model.

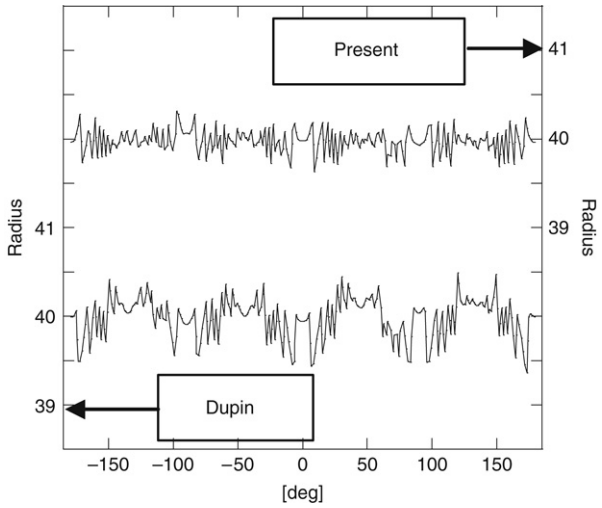

Fig. 2. Drop radius as a function of positions on the perimeters of the droplets. A strong fluctuation is observed in the result of the Dupin model. Note that the vertical axes are shifted to have a clearer view.

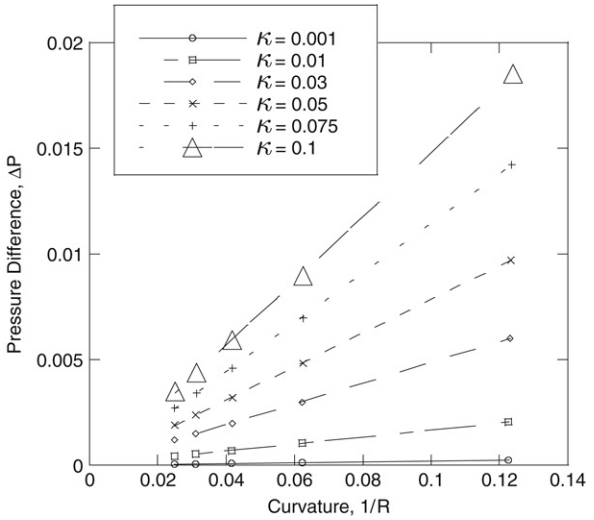

Fig. 3. Pressure differences inside and outside of the drops are plotted against the curvatures of drops (the inverse drop radius).

In Fig. 2, the droplet radius is plotted as a function of azimuthal angle. Note that the plots are shifted for a clearer view, so that the left vertical axis is for the Dupin model while the right one is for our model. Obviously, the fluctuation of radius is smaller in the present model. These results indicate the developed fluid–fluid interface tension model can make the interface more realistic than the Dupin model.

We further investigated the relationship between the curvature (the inverse drop radius) $1/R$ and the pressure difference inside and outside the droplet ΔP under the condition that the interaction parameter κ is kept constant. The results obtained with different values of κ are shown in Fig. 3. The symbols are the simulation results and the lines are drawn as the least-square linear fitting of them. They clearly satisfy the Laplace's law, $\Delta P \propto 1/R$, for all the values of κ.

With the use of the Laplace's law, we can calculate the interfacial tension coefficients σ, and plotted them against κ in Fig. 4. It is observed that the interface tension σ is almost proportional to the interface tension parameter κ.

The verification of the Laplace law for a single droplet shown above indicates that the developed interface tension model can handle the interface tension correctly, and that a wide range of values can be chosen for the interface tension coefficients.

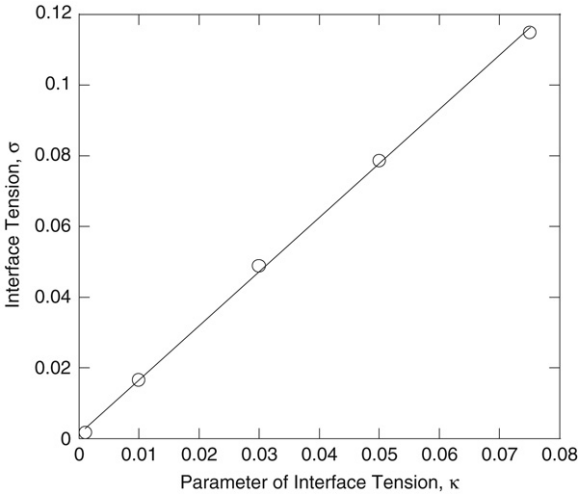

Fig. 4. The interface tension σ as a function of the interface tension parameter κ.

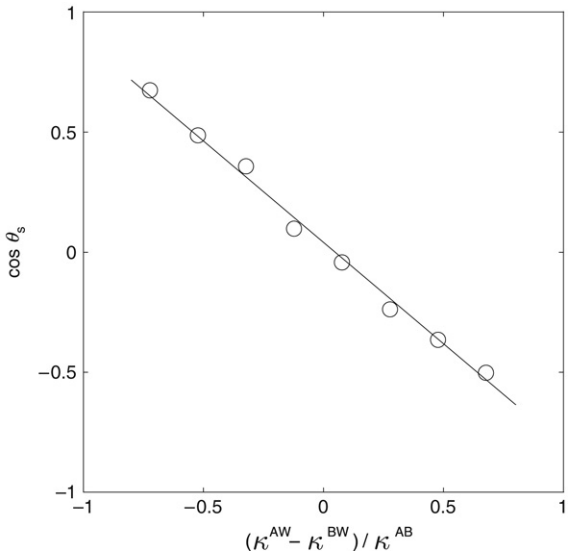

Fig. 5. The contact angles obtained when different values of fluid–solid interaction parameters, κ^{AW} and κ^{BW} are used.

3.2. Static contact angles

To demonstrate the applicability of the developed model for wetting properties, we simulated a droplet attached on a solid wall, and measured contact angles in the static states.

In Fig. 5, the results are plotted as a function of $(\kappa^{AW} - \kappa^{BW})/\kappa^{AB}$, where κ^{AW} and κ^{BW} are the parameters for controlling the interfacial tensions between the fluid phase A and the solid wall and that between the fluid phase B and the solid phase, respectively. Note that the parameter for controlling the interfacial tension between fluid A and fluid B, κ^{AB}, is kept constant. The solid line is the least-square linear fitting of the obtained data. It shows that the cosines of the contact angles are in a linear relation with the difference of the interfacial interaction parameters $(\kappa^{AW} - \kappa^{BW})/\kappa^{AB}$.

This linear relation found in the simulation may be compared with the Young's equation [14],

$$\cos\theta_S = -\frac{\sigma^{AW} - \sigma^{BW}}{\sigma^{AB}}, \tag{16}$$

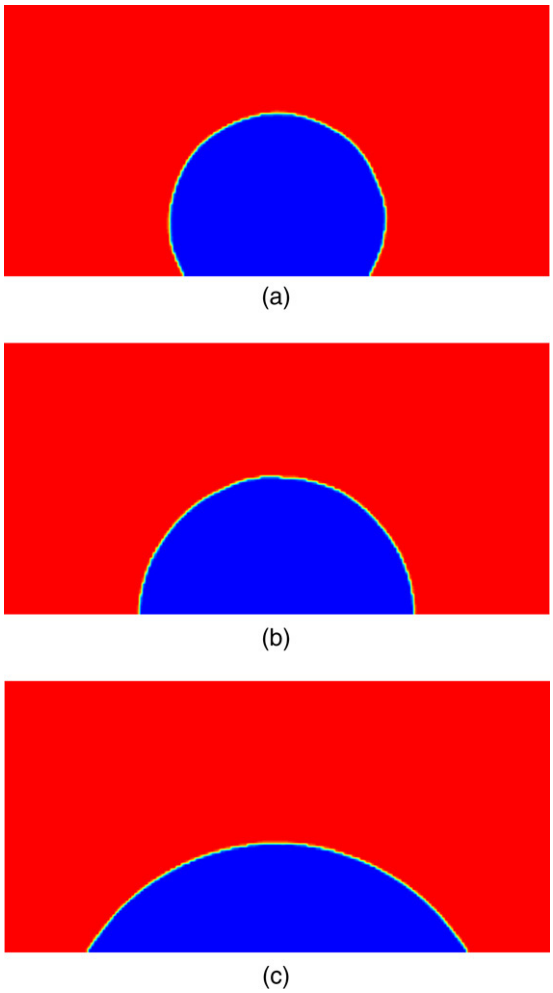

Fig. 6. The drops with different contact angles.

where σ^{AW} is the interface tension working at the interface between the fluid phase A and the solid wall, and so on. However, as mentioned before, the relation between κ^{AW} and σ^{AW} (or κ^{BW} and σ^{BW}) is not yet clear, though the relation has been already established for fluid phases (see Fig. 4). Nevertheless, the obtained results are qualitatively correct. Therefore, the developed model is very useful to treat the wettability. As examples, we show the shapes of the droplets in Fig. 6 whose contact angles are 60°, 90° and 120° in the steady states. It is also observed that the fluid–fluid interface draws a fair circular arc, showing the effectiveness of the modeling of interfacial tensions.

3.3. Dynamic contact angles

Droplets attached on a wall in shear flows are simulated to investigate the characteristics of contact-line motions. We examined the advancing contact angle θ_A, the receding contact angle θ_R and the droplet velocity V_{drop} when the shear flows are driven by moving the upper wall at a constant velocity V_{wall}. As shown in Fig. 7, the advancing contact angle is defined as the angle measured from the droplet side of the contact line, and the receding contact angle is defined as the angle measured from the bulk fluid side of the contact line.

Reynolds number and capillary number are defined as follows:

$$Re = \frac{\rho U L}{\mu}, \qquad Ca = \frac{\mu U}{\sigma}, \tag{17}$$

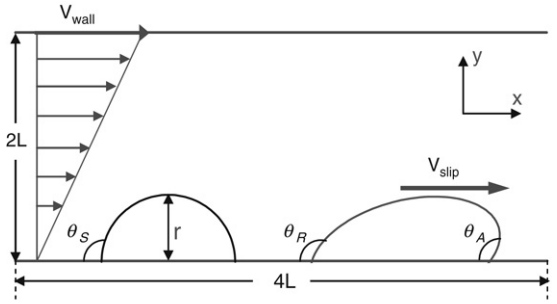

Fig. 7. A schematic illustration of the simulation geometry. The droplet on the left is in the original shape before the start of flow, while the one on the right is deformed by the shear flow.

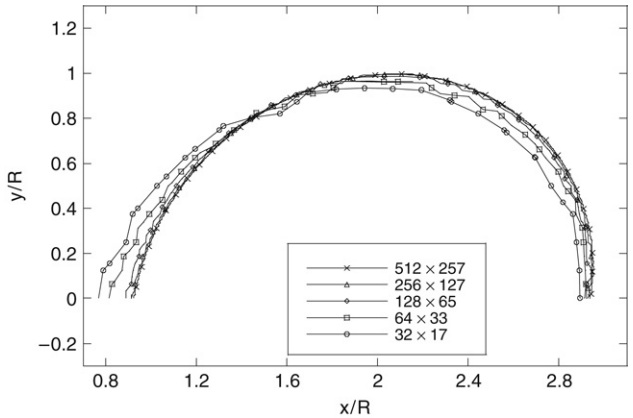

Fig. 8. Droplet shapes in the steady states when $Re = 0.6$ and $Ca = 0.1$, simulated with different lattice resolutions. It is observed that the droplet shapes converge toward the result obtained with the highest lattice resolution.

where μ is the viscosity. The characteristic velocity U is taken as the flow velocity at the top of the drop to estimate inertial and viscous forces exerted on the drop, and is defined as $U = rV_{\text{wall}}/2L$ with the distance between the upper and the lower walls $2L$ and the initial height of the droplet r. Note that the periodic condition is used for the lateral direction.

To confirm the convergence of the developed model, simulations for $Re = 0.6$ and $Ca = 0.1$ were carried out on the following lattice configurations: 32×17, 64×33, 128×65, 256×129 and 512×257. Note that viscosity was fixed as $\mu = 1/6$ for all the cases.

Fig. 8 shows the shapes of the droplets in steady states obtained with each lattice configurations. Shapes of all the droplets are almost the same and it can be found that the droplet shapes converge toward the result obtained with the highest lattice resolution. To evaluate the convergence quantitatively, the relative error of the arc length,

$$E_{\text{arc}} = \frac{L - L_r}{L_r} \tag{18}$$

and that of the order parameter,

$$E_{\text{order}} = \frac{\sqrt{\sum_{\vec{x}} (\phi(\vec{x}) - \phi_r(\vec{x}))^2}}{\sqrt{\sum_{\vec{x}} \phi_r^2(\vec{x})}} \tag{19}$$

were calculated. Here, the subscript r indicates the reference values, namely the results obtained with the finest lattice resolution 512×257. The summation is taken over the whole corresponding grid points in the coarser lattice

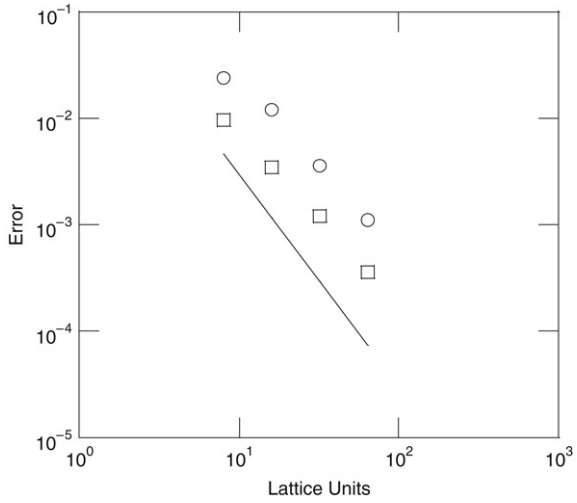

Fig. 9. The convergence rate for $Re = 0.6$ and $Ca = 0.1$. The errors are calculated relative to the results obtained on the 512×257 lattice configuration. The circles are for E_{order}, and the squares are for E_{arc}. The solid line shows a reference for the second-order convergence rate.

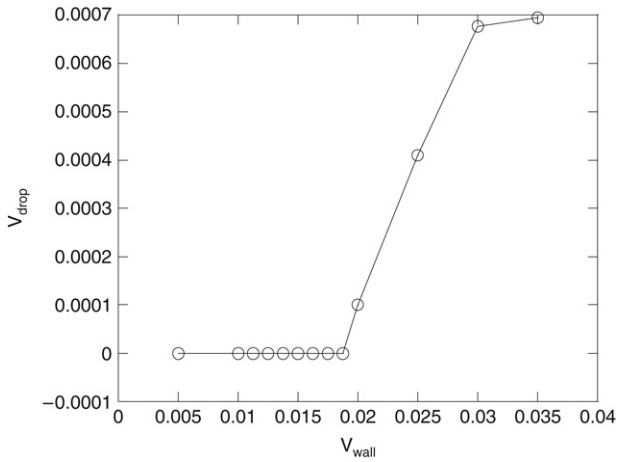

Fig. 10. Droplet velocity vs. wall velocity.

configurations. To calculate the arc length L, we firstly draw isoline of $\phi = 0.5$ using the Marching Cube method [15], and sum up the lengths of all the segments.

The relative errors E_{arc} and E_{order} are plotted in Fig. 9. The solid line shows the second-order convergence rate. The convergence rates of both the arc length and the order parameter are a little less than the second order.

Next, we investigated the relationship between droplet velocity V_{drop} and the wall velocity V_{wall}. The simulations below are carried out under the following conditions, the lattice size is 512×128, the initial droplet height is $r = 32$, the static contact angle is $\theta_S = 90°$, the controlling parameter for the fluid–fluid interface tension is $\kappa^{AB} = 0.012$, and the viscosity is $\mu = 1/3$.

The results are shown in Fig. 10. Note that $\kappa^{AW} = \kappa^{BW} = 0$ in this case. The motions of the droplet can be classified into three modes. The first is the stationary mode where the droplet deforms but stays still. Note that the contact angles θ_A and θ_R are changed from the static contact angle $\theta_S = 90°$. The second is the slip mode where the droplet slips and steady states exist for the droplet shape and the droplet velocity. In this region, the slipping velocity varies linearly to the wall velocity. And the final is the breakup mode where the droplet is divided into two pieces. The droplet shape in each mode is shown in Fig. 11(a), (b) and (c) respectively.

The relationship between the droplet velocity V_{drop} and the dynamic contact angle θ_A and θ_R is shown in Fig. 12. It is observed again that the droplet can stay still even though both contact angles θ_A and θ_R deviate from the static

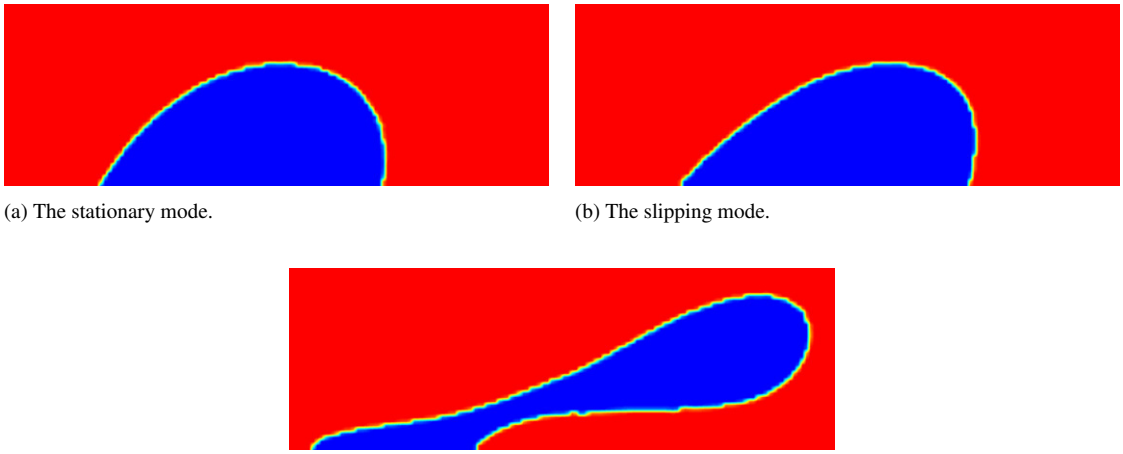

(a) The stationary mode.

(b) The slipping mode.

(c) The breakup mode.

Fig. 11. Three modes of the drop motion are observed in the simulations.

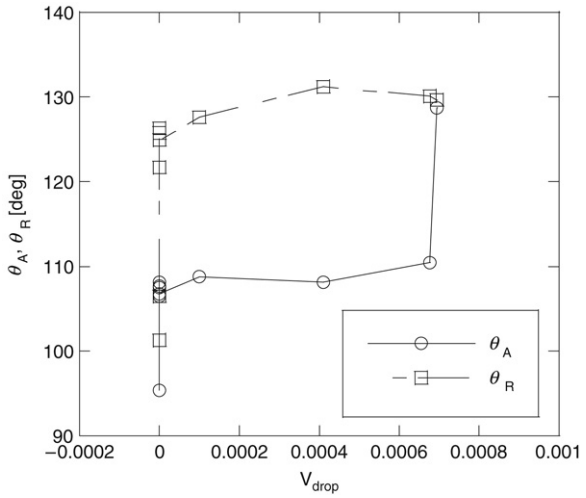

Fig. 12. Dynamic contact angles vs. drop velocity. The fluid–solid interactions parameters are set $\kappa^{AW} = \kappa^{BW} = 0.0$, so that the static contact angle is set to be 90°.

contact angle $\theta_S = 90°$. This phenomenon has been observed in many experiments, and is known as the contact-angle hysteresis [16]. From the observation above, it can be said that the developed model can reproduce this hysteresis phenomenon.

To investigate the influence of the fluid–solid interface tension on the contact-angle hysteresis phenomenon, we performed simulations with the same configurations, but with different controlling parameters for the solid–fluid interfacial tensions, κ^{AW} and κ^{BW}.

Fig. 13(a) and (b) are the results when $\kappa^{AW} = \kappa^{BW} = 0.02$ and -0.02. Note that the static contact angles are 90° in both cases. There is no significant difference in the advancing contact angles, but the receding contact angles in Fig. 13(b) are smaller. Hence it indicates that the droplet moves at the same velocity with smaller deformation when the droplet has smaller interface tension with the solid wall.

From these analyses, we can give the following comments: The static contact angles are determined, following Young's formula, from the fluid–fluid interface tension and the difference of fluid–solid interface tensions. On the other hand, the dynamic contact angles depend not only on the difference of fluid–solid interface tensions but also on the absolute values of the two fluid–solid interface tensions. The latter statement cannot be verified at the moment, however, due to the difficulty in measuring the fluid–solid interfacial tensions.

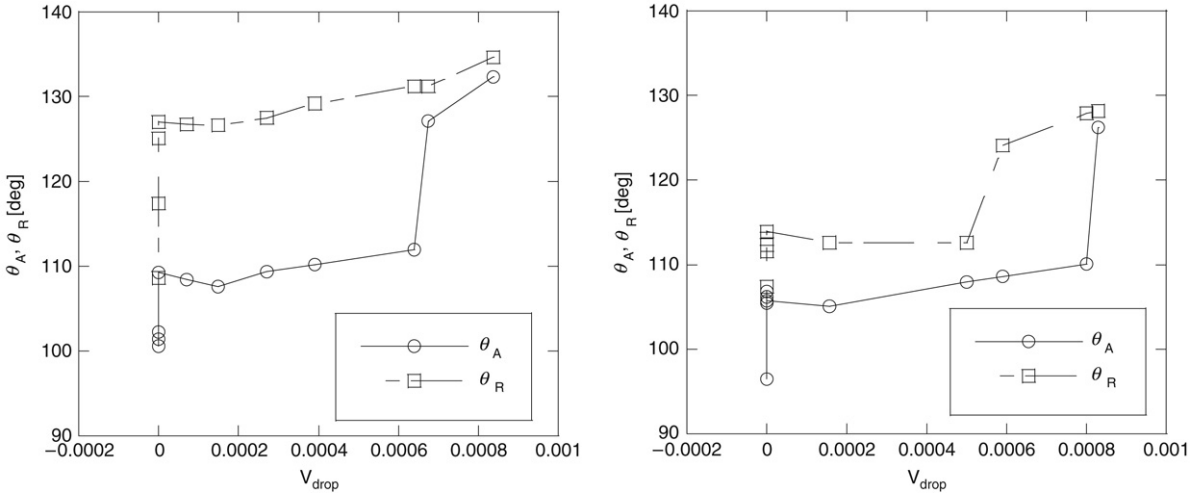

(a) $\kappa^{AW} = \kappa^{BW} = 0.02$. (b) $\kappa^{AW} = \kappa^{BW} = -0.02$.

Fig. 13. Dynamic contact angles vs. drop velocity, with different fluid–solid surface tension controlling parameters.

4. Conclusions

Using the developed model for contact-line motions one can reproduce the hysteresis phenomena without the implementation of the slip model, like what was done in the continuum mechanics based simulations. In addition, it is shown that the dynamic contact angle depends not only on the droplet velocity but also on the absolute value of the fluid–solid interface tension. As a preliminary work, we only simulated the contact-line motions in 2D, with a static contact angle of 90°. Note that the static contact angle can be varied by adjusting each controlling parameter of the fluid–solid interface tension independently. Simulations of contact-line motions with different static contact angles in 3D, as well as a further comparison with the experimental and theoretical results will be done in the future work.

References

[1] A.K. Gunstensen, D.H. Rothman, S. Zaleski, G. Zanetti, Lattice Boltzmann model of immiscible fluid, Phys. Rev. A 43 (1991) 4320–4327.
[2] V.E.B. Dussan, On the spreading of liquids on solid surfaces: Static and dynamic contact lines, Annu. Rev. Fluid Mech. 11 (1979) 371–400.
[3] P.D.M. Spelt, A level-set approach for simulations of flows with multiple moving contact lines with hysteresis, J. Comput. Phys. 207 (2005) 389–404.
[4] A.D. Schleizer, R.T. Bonnecaze, Displacement of a two-dimensional immiscible droplet adhering to a wall in shear and pressure-driven flows, J. Fluid Mech. 383 (1999) 29–54.
[5] A.J. Briant, A.J. Wagner, J.M. Yeomans, Lattice Boltzmann simulations of contact line motion. I. Liquid–gas systems, Phys. Rev. E 69 (2004) 031602.
[6] A.J. Briant, J.M. Yeomans, Lattice Boltzmann simulations of contact line motion. II. Binary fluids, Phys. Rev. E 69 (2004) 031603.
[7] S. Chen, G.D. Doolen, Lattice Boltzmann method for fluid flows, Annu. Rev. Fluid Mech. 30 (1998) 329–364.
[8] X. Shan, H. Chen, Lattice Boltzmann model for simulating flows with multiple phases and components, Phys. Rev. E 47 (1993) 1815–1819.
[9] M.R. Swift, E. Orlandini, W.R. Osborn, J.M. Yeomans, Lattice Boltzmann simulations of liquid–gas and binary fluid systems, Phys. Rev. E 54 (1996) 5041–5052.
[10] M.M. Dupin, I. Halliday, C.M. Care, Multi-component lattice Boltzmann equation for mesoscale blood flow, J. Phys. A 36 (2003) 8517–8534.
[11] D. Kehrwald, Numerical analysis of immiscible lattice BGK, Doctoral Dissertation of the University of Kaiserslautern, 2002.
[12] B. Lafaurie, C. Nardone, R. Scardovelli, S. Zaleski, G. Zanetti, Modelling merging and fragmentation in multiphase flows with SURFER, J. Comput. Phys. 113 (1994) 134–147.
[13] I. Ginzburg, G. Wittum, Two-phase flows on interface refined grids modeled with VOF, staggered finite volumes, and spline interpolants, J. Comput. Phys. 166 (2001) 302–335.
[14] J. Israelachvili, Intermolecular & Surface Forces, Academic Press, 1992.
[15] W.E. Lorensen, H.E. Cline, Marching cubes: A high resolution 3D surface construction algorithm, Comput. Graph. 21 (1987) 163–170.
[16] V.E.B. Dussan, R.T.-P. Chow, On the ability of drops or bubbles to stick to non-horizontal surfaces of solids, J. Fluid Mech. 137 (1983) 1–29.